ISSN (Print) 1226-1750
ISSN (Online) 2233-6656
Journal of Magnetics 25(2), 140-149 (2020) https://doi.org/10.4283/JMAG.2020.25.2.140

Fabrication, Structure, and Magnetic Properties of Pure-Phase $BiFeO_3$ and $MnFe_2O_4$ Nanoparticles and their Nanocomposites

Inna Yusnila Khairani[1], Anindityo Nugra Arifiadi[1], Jae-Hyeok Lee[1], Biswanath Bhoi[1], Sandeep Kumar Singh Patel[2], and Sang-koog Kim[1]*

[1]National Creative Research Initiative Center for Spin Dynamics and Spin-Wave Devices, Nanospinics Laboratory, Research Institute of Advanced Materials, Department of Materials Science and Engineering, Seoul National University, Seoul 08826, Republic of Korea
[2]Department of Chemistry, MMV, Banaras Hindu University, Varanasi- 221005, India

(Received 3 March 2020, Received in final form 20 June 2020, Accepted 23 June 2020)

We fabricated pure-phase $BiFeO_3$ (BFO) and $MnFe_2O_4$ (MFO) nanoparticles as well as their nanocomposites (BMFO), and then we studied their structures and magnetic properties. Pristine BFO nanoparticles of 93.3 nm average diameter were successfully synthesized using the sol-gel method by varying the solvent condition and the precursor amount. Pristine MFO nanoparticles with a mean diameter of 70.5 nm were synthesized using the co-precipitation method entailing the optimization of the preheating and aging steps. The fabricated MFO nanoparticles showed mostly nanospheres with few nanocubes. The nanocomposite samples of 50 % MFO and 50 % BFO were fabricated through grinding and pelletization, followed by sintering under an inert atmosphere. The crystal structures of the pristine materials in the nanocomposites were well preserved. The magnetization values (M_s) of the BFO, MFO, and BMFO were 4.9, 52, and 33 emu/g, respectively. This latter M_s value was significantly higher than that of BFO, owing to the coexistence of Fe^{2+} and Fe^{3+} in its BFO phase and the incorporation of magnetic MFO. Two synthesis methods and material properties including the structural, morphological, magnetic, and oxidation states of the BFO-MFO nanocomposites were studied in order to achieve a high M_s value of 33 emu/g, which is higher than the bulk values of previously reported BFO-MFO composite samples.

Keywords : $BiFeO_3$, $MnFe_2O_4$, nanocomposites, sol-gel, co-precipitation, magnetic properties

1. Introduction

Multiferroic materials have attracted great attention due to their potential applications to spintronic devices [1-3]. Among many candidates, $BiFeO_3$ (BFO) is considered to be the most promising material owing to its ferroelectric Curie temperature of $T_C \approx 1143$ K and antiferromagnetic Neel temperature of $T_N \approx 640$ K, both of which are much higher than room temperature [4, 5]. Compared with other materials, BFO has a large electric polarization and noticeable magnetoelectric coupling at room temperature [4, 6]. However, its practical application is still limited due to its low magnetic moment arising from antiferromagnetic G-type spin ordering along its $[001]_{hex}$ axis, superimposed by an incommensurate cycloidal spin configuration propagating along the $[110]_{hex}$ axis with a periodicity of 62 nm [7, 8]. In order to tackle this obstacle, a few methods have been proposed to make it ferromagnetic or ferromagnetic-like. Synthesis of nano-size BFO of less than 62 nm can be employed to suppress the spiral spin structure in order to increase the contribution of uncompensated spins at the surface or interface [9]. Another way is to introduce structural phase transformation by substituting Bi^{3+} or Fe^{3+} ions with rare earth ions (e.g. Pr^{3+}, Tb^{3+}, Dy^{3+}, Gd^{3+}), transition metal ions (e.g. Mn^{2+}, Co^{2+}) or multi-ion co-doping (e.g. La^{3+}-Co^{2+}, Pr^{3+}-Co^{2+}) [10-17]. Additionally, BFO can be composited with other, higher-magnetization-value materials such as spinel ferrites (e.g. $CoFe_2O_4$, $NiFe_2O_4$, $ZnFe_2O_4$, $MnFe_2O_4$) [18-21].

To our best knowledge, there have been no reports on pure-phase spinel $BiFeO_3$ or perovskite $MnFe_2O_4$ (MFO) nanocomposites. Therefore, in this study, we chose MFO to enhance the magnetic properties of BFO by rendering these two pure-phase materials as composites (i.e., BFO-MFO). It has been reported that low coercivity is beneficial for enhancement of multiferroic properties [22] and

©The Korean Magnetics Society. All rights reserved.
*Corresponding author: Tel: +82-2-880-1458
Fax: +82-2-880-1457, e-mail: sangkoog@snu.ac.kr

© 2020 Journal of Magnetics

that phase purity is important, especially for the suppression of the leakage current of BFO [23]. In this regard, in the present study, we investigated the fabrication, structure and magnetic properties of BFO-MFO nanocomposites starting from the synthesis of pure-phase MFO and BFO nanoparticles.

2. Experimental Procedure

2.1. Synthesis of Pure-Phase BFO Nanoparticles

Pure-phase BFO nanoparticles were fabricated using the typical sol-gel synthesis method with propylene glycol as the chelating agent. To make 2 mmol of BFO, around 0.97014 g of $Bi(NO_3)_3 \cdot 5H_2O$ was dissolved in 20 mL of water and 1 mL of HNO_3 was added to help the solvation of the white insoluble bismuth oxynitrate. The mixture was then stirred to facilitate the dissolution of bismuth nitrate salt. Subsequently, 0.808 g of $Fe(NO_3)_3 \cdot 9H_2O$ was added to the mixture, and the solution was stirred at room temperature. After complete dissolution, the solution was heated, and 1 mL of propylene glycol was added to form the sol-gel. The mixture was then heated at 100 °C until the sample was completely dried. The dried powder was subsequently ground and annealed in an ambient atmosphere at 400 °C for 2 hours at a heating rate of 3 °C/min. The pure phase of the BFO nanoparticles was obtained after annealing.

2.2. Synthesis of Pure-Phase MFO Nanoparticles

MFO (10 mmol) was synthesized using the co-precipitation method. Metal salts at a molar ratio of 1:2 (Mn:Fe) were mixed in 100 mL of DI water and stirred at room temperature for more than 3 hours. The mixture was then preheated to 80 °C and stirred for 15 minutes. Boiling NaOH solution was then added dropwise as precipitant until the pH of the solution was within the 12-14 range. The color of the mixture turned from light brown to dark brown as the pH increased. After the desired pH was reached, the mixture was aged at 95-100 °C to evaporate the solvent. The obtained dark-brown precipitates were later washed with DI water using magnetic decantation until the pH was 7. After that, the precipitates were washed one more time with ethanol aided by centrifugation to remove unwanted residues. The precipitates were then dried at 100 °C for 12 hours using an oven to obtain MFO nanoparticle powder.

2.3. Fabrication of BFO-MFO Nanocomposite Samples

Polyvinyl alcohol (PVA) solution (2 %) was prepared, and the appropriate amounts of BFO and MFO powder were mixed at the 1:1 molar ratio by adding a few drops of acetone. The pellet was fabricated by pressing the mixed powder using a uniaxial hydraulic press. The composite was pressed up to 6000 psi to produce a very small and thin pellet with a diameter of 1 cm and a thickness of 0.5-1 mm. The pellet was sintered at 400 °C for 2 hours in N_2 atmosphere at a heating rate of 3 °C/min and then naturally cooled. The composite was polished and coated with Pt prior to field-emission scanning electron microscopy (FESEM) analysis.

2.4. Characterizations of Structural and Magnetic Properties

The crystallinity and phase of the samples were examined by X-ray diffraction (XRD, D8 Advance, Bruker Miller Co.) using the CuKα wavelength (λ = 1.5406 Å). The morphology was observed using high-resolution transmission electron spectroscopy (HR-TEM, JEM-2100F, JEOL Ltd) operated at 200 kV and FESEM (JSM-7600F, JEOL). The magnetic property was measured using a vibrating sample magnetometer (VSM-7410, Lake Shore) at room temperature (300 K). Finally, the oxidation state of the sample was determined using X-ray photoelectron spectroscopy (XPS, Axis-HSI Instrument, Kratos Inc.).

3. Results and Discussion

3.1. Synthesis of Pure-Phase BFO Nanoparticles

3.1.1. Effect of solvent condition on synthesis of pure-phase BFO nanoparticles

In the synthesis of pure-phase perovskite BFO, we discovered that the solvent condition is integral to sample purity. Figure 1 shows the XRD patterns of the samples synthesized without (black line) the addition of HNO_3 and with of 2, 4 and 6 mmol of HNO_3 mmol (blue, red and green lines, respectively). In the sample without the addition of HNO_3, the impurity phase of bismuth oxide (Bi_2O_3) is present as a side product of the annealed bismuth oxynitrate $Bi[(OH)_2(NO_3)]$. The white insoluble compound of $Bi[(OH)_2(NO_3)]$ was produced during the synthesis as the hydrolysis product of bismuth nitrate salt $Bi(NO_3)_3$ according to the following reaction [24]:

$$Bi(NO_3)_3 + 2H_2O \rightleftharpoons Bi[(OH)_2(NO_3)] + 2HNO_3$$

Due to this reaction, the addition of HNO_3 followed by stirring is required to shift the balance and ensure the complete solvation of $Bi[(OH)_2(NO_3)]$. It should be noted that the addition of water also promotes further hydrolysis of $Bi(NO_3)_3$, leading to the formation of insoluble salt bismuth hydroxide $Bi(OH)_3$ [25]. Therefore, a minimum amount of water should be used to ensure easier solvation

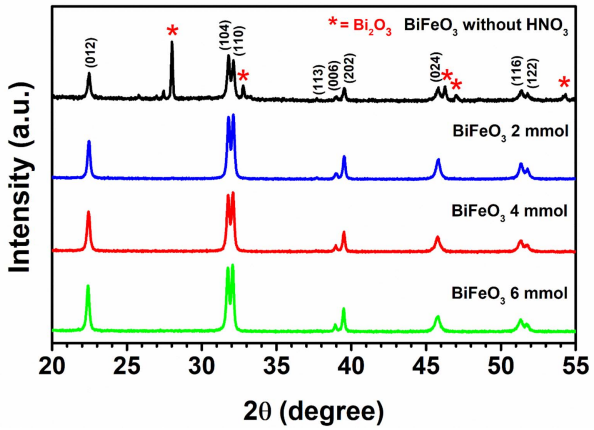

Fig. 1. (Color online) XRD patterns of $BiFeO_3$ particles fabricated without addition of HNO_3 (top) and according to variation of precursor amount of $BiFeO_3$ (2, 4, and 6 mmol).

of the bismuth salt. It should also be noted that a larger batch of $Bi(NO_3)_3$ should be accompanied by a larger amount of nitric acid, as the inadequacy of HNO_3 may lead to the formation of Bi_2O_3 as the end-product. The HNO_3 addition should be excessive in order to ensure complete dissolution according to the following reaction:

$$Bi[(OH)_2(NO_3)] + H_2O \rightleftharpoons Bi(OH)_3 + HNO_3$$

The other important aspect besides the solvent condition is the precursor quantity, which was found to influence the particle size of BFO. Bismuth ferrites were prepared with different precursor amounts (2, 4, and 6 mmol), and all of the samples showed the same XRD pattern (Fig. 1. blue, red, and green lines), indicating successful synthesis of single-phase BFO. The average crystallite sizes of the powders were calculated using the Debye-Scherrer equation [26], resulting in 34.0, 34.4, and 37 nm for the 2, 4, and 6 mmol precursor amounts, respectively. The increase of the crystallite size was caused by the higher concentration of the precursor, which can be explained by classical nucleation theory: as the critical concentration of the precursor is achieved, nucleation takes place and nuclei will be formed; the unused precursor is then used as sustenance to grow the nuclei into larger particles; the higher the precursor concentration, the faster the particle growth. Thus, the 6 mmol precursor amount, which had the highest precursor concentration, showed the largest crystallite size (37 nm), followed by 4 and 2 mmol with 34.4 and 34.0 nm, respectively.

3.1.2. Morphology, structure and magnetic analysis of BFO

The morphologies of the samples were examined to understand the effect of precursor amount on the shape

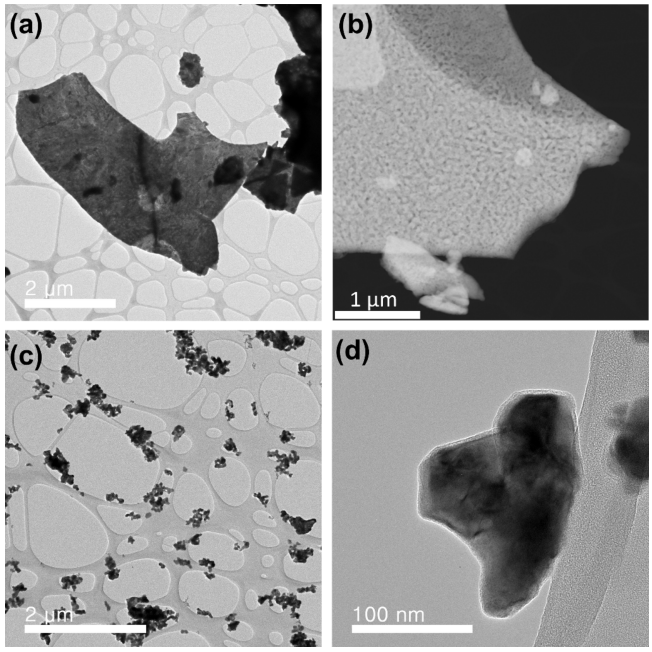

Fig. 2. TEM images of 6 mmol $BiFeO_3$ (a-b) and 2 mmol $BiFeO_3$ (c-d).

and size of BFO particles. In Fig. 2(a), the TEM bright-field image of 6 mmol BFO shows that the BFO was formed as flat, micro-size sheets, while the image of 2 mmol BFO indicates that it was produced as nanoparticles (Fig. 2(c and d)). For a clearer view of the 6 mmol sample, an image was taken using a high angle diffraction mode (Fig. 2(b)). In this mode, the sample appears in high contrast (white), while parts with less BFO appear darker. Interestingly, the formed flat sheets of the 6 mmol BFO actually contained pores, which probably came from the severely agglomerated nanoparticles that were bound together as sheets. This result indicates that the sol-gel method can produce nanoporous BFO sheets without the need of a template.

The magnetization hysteresis loop of the sample powder was measured at room temperature to understand the influence of precursor amount on magnetic properties. In Fig. 3, it is clear that the 6 mmol sample produced a much higher saturation magnetization (M_s) value (7.7 emu/g) than did the 2 mmol sample (only 4.9 emu/g). It was comparatively higher than some of the formerly fabricated sol-gel synthesized BFO samples as well [27-30]. Earlier work reported that the increase of BFO magnetization might be related to the presence of a particularly small amount of Fe_3O_4 in the system [27]. To investigate this phenomenon, slow-scan XRD (0.2°/min speed) was conducted in the 35-36° range. According to the result (Supplementary Fig. S1), no trace of the strongest (311) peak of Fe_3O_4 impurity was found in the sample.

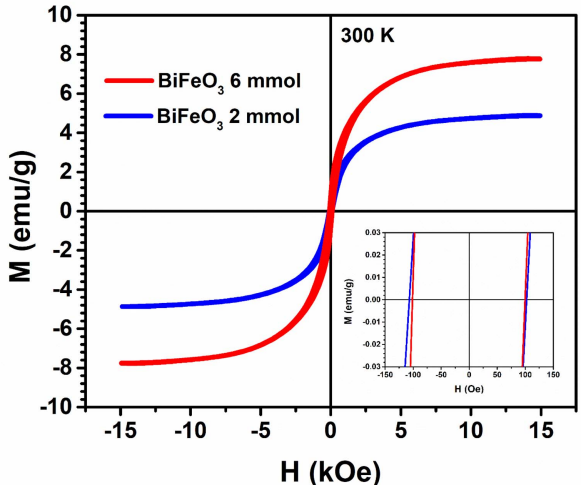

Fig. 3. (Color online) Magnetic hysteresis loops for $BiFeO_3$ samples with 6 mmol (red) and 2 mmol (blue) precursor amounts (inset: zoomed loops near coercivity values).

Another comparative sample emphasizes the absence of Fe_3O_4 in the BFO sample, as a peak can be observed at around 35.6°. It can be concluded that the BFO powder synthesized by this procedure does not contain Fe_3O_4 impurities that may contribute to a large magnetization value.

To elucidate whether the magnetization increase was caused by the presence of Fe^{2+} [31, 32], the XPS spectra were measured. As seen in the inset of Fig. 4, the supposed Fe^{3+} main $2p_{3/2}$ peak at around 711 eV was slightly shifted to the smaller binding energy of 710.6 eV for the 2 mmol sample, and to 709.5 eV for the 6 mmol sample. This fact indicates the presence of Fe^{2+} in the system.

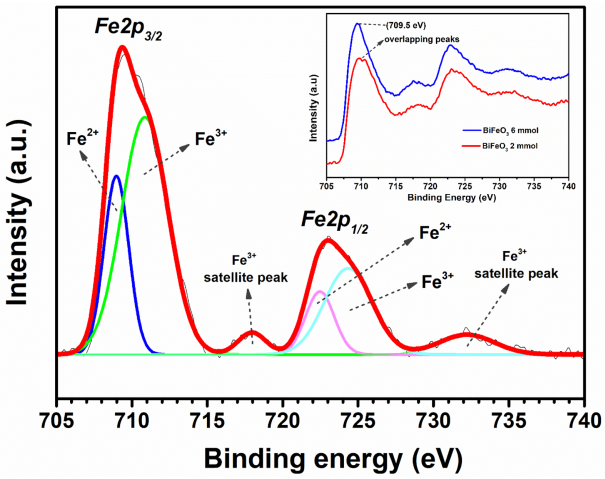

Fig. 4. (Color online) XPS spectra of $BiFeO_3$ (fabricated with 2 mmol precursor amount) fitted using Gaussian profile in binding-energy regions of $Fe2p_{3/2}$ and $Fe2p_{1/2}$ (inset: comparison of BFO 6 mmol and 2 mmol).

Further peak fitting analysis of the 2 mmol BFO sample showed the coexistence of Fe^{3+} and Fe^{2+} peaks at the corresponding binding energies of 710.9 and 709 eV, respectively. The presence of the Fe^{2+} $2p_{1/2}$ peak was also observed at 722.5 eV, accompanied by the $2p_{1/2}$ peak of Fe^{3+} at 724.4 eV. Meanwhile, the satellite peaks indicated only the presence of Fe^{3+}, due to the more dominant presence of Fe^{3+}. The XPS results showed that the increased magnetization of 2 and 6 mmol of BFO was caused by the presence of Fe^{2+} in the system. The reduction of the ratio of Fe^{3+} to Fe^{2+} might cause a structural distortion due to the larger size of the Fe^{2+} ions and the chance of a double-exchange interaction between Fe^{2+} and Fe^{3+} [31], which is likely to arise in BFO samples [33] typically prepared by sol-gel method, due specifically to the annealing in air atmosphere [34]. According to the calculated area below the peaks, the ratios of the Fe^{3+} and Fe^{2+} concentrations of 2 and 6 mmol BFO were approximately 2.5:1 and 1.4:1 (Supplementary Fig. S2, Table S1), respectively. These results indicate that the concentration of Fe^{2+} in the BFO synthesized with 6 mmol of precursor amount was higher than that in the BFO prepared with 2 mmol of precursor amount. They prove, in other words, that the phenomenon of the increased magnetization of the 6 mmol BFO sample relative to 2 mmol BFO was due to the presence of Fe^{2+} in the system.

3.2. Synthesis of Pure-Phase MFO Nanoparticles

3.2.1. Preheating step

Spinel MFO nanoparticles were fabricated using the co-precipitation method. This method works by adding precipitant (e.g. NaOH or NH_4OH) to the solution of the metal source until a certain pH value is reached. Subsequent heating also is required, to promote the formation of metal oxides from the metal hydroxides that are produced after precipitant addition through dehydration and atomic rearrangement [35]. The equation below shows the synthesis reaction of manganese ferrite via the co-precipitation method:

$$2Fe^{3+} + Mn^{2+} + 8OH^- \rightleftharpoons Mn(OH)_2 + 2Fe(OH)_3$$
$$\rightarrow MnFe_2O_4 + 4H_2O$$

In the co-precipitation method, many factors, including the precursor condition, synthesis temperature, time, and pH level, influence the properties of the synthesized product. We compared the result for the sample that was preheated for 15 minutes at 80 °C with that for the sample without preheating. In the XRD patterns shown in Fig. 5, the preheated sample shows no peak that corresponds to the impurity of iron oxide at $2\theta = 36°$, while the iron oxide peak is still observable in the sample without the

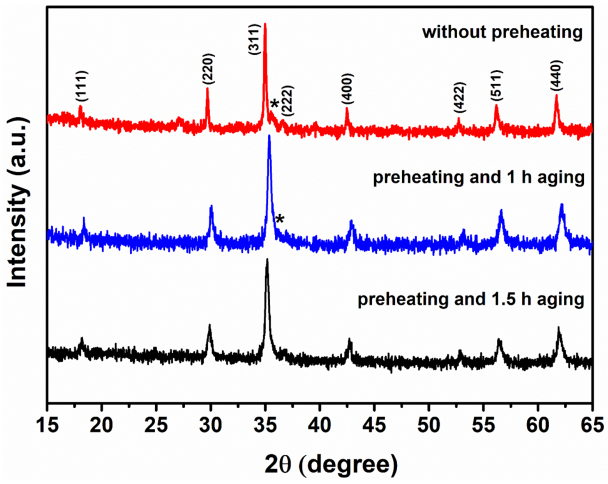

Fig. 5. (Color online) XRD patterns of $MnFe_2O_4$ sample fabricated without preheating (top, red), with preheating and subsequent aging for 1 h (middle, blue) and 1.5 h (bottom, black).

preheating step. Mixing the precursor solution and precipitant at an increased temperature is believed to increase the clustering and growth of the particles and to promote the formation of monodisperse particles [36]. This condition of particle congregation at an increased temperature might increase the collision probability between metal hydroxides, thus reducing the formation of iron oxide impurities from uncollided iron hydroxide.

3.2.2. Effect of aging step on synthesis of pure-phase MFO nanoparticles

After the sample preparation, the sample for 1.5 h aging showed a more resolved peak at $2\theta = 36.62°$ than did the sample for 1 h aging (see Fig. 5). Samples for shorter aging times have been reported to contain intermediate phases of FeOOH and metal hydroxides [37]. Since aging promotes dehydration of hydroxides and atomic rearrangement for the formation of spinel ferrite [35], the longer the aging time, the more time is given for dehydration and transformation to take place, which condition consequently reduces the products of the intermediate phases. This results in the elimination of iron oxide impurities, as shown by the XRD peak at $2\theta = 36^o$ for the sample with 1.5 h aging (Fig. 5).

3.3. Structural, Morphological, Oxidation and Magnetic Properties

3.3.1. Structural properties

The XRD results shown in Fig. 6(a) indicate successful fabrication of single-phase rhombohedral BFO with the R3c space group (PDF No. 01-080-3418), while the lattice parameters in Table 1 show similar results to those of the

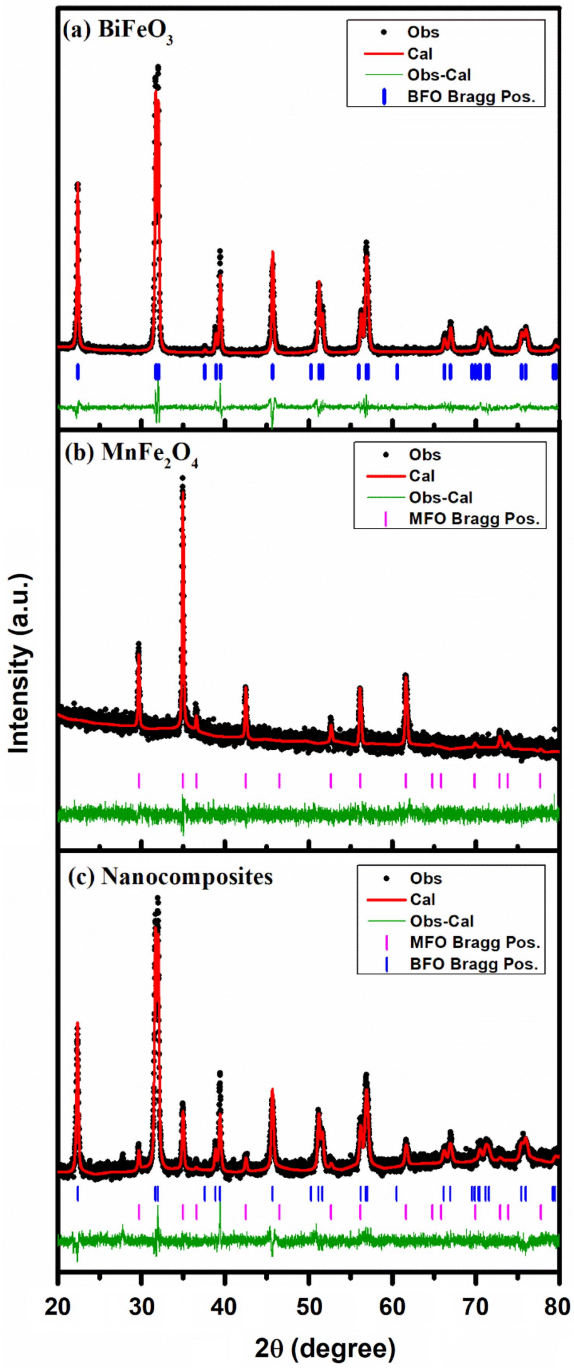

Fig. 6. (Color online) Rietveld refinements of XRD patterns of (a) $BiFeO_3$, (b) $MnFe_2O_4$, and (c) $MnFe_2O_4$-$BiFeO_3$ nanocomposites.

BFO database. Meanwhile, the average crystallite size calculated using the Debye-Scherrer equation was found to be 31.9 nm.

The XRD result for the final MFO sample that was obtained from the optimum synthesis conditions is shown in Fig. 6(b). The Rietveld refinement of XRD patterns shows a well-fitted spinel structure attributable to the

Table 1. Parameters of crystal structures obtained from Rietveld refinements of XRD spectra of $BiFeO_3$, $MnFe_2O_4$, and their nanocomposite.

Parameters	$BiFeO_3$	$MnFe_2O_4$	Nanocomposite	
			$BiFeO_3$	$MnFe_2O_4$
Crystal structure	Rhombohedral	Cubic	Rhombohedral	Cubic
Space group	R3c	Fd-3m	R3c	Fd-3m
a (Å)	5.5752(2)		5.5863(2)	
b (Å)	5.5752(2)	8.5020(5)	5.5863(2)	8.5002(6)
c (Å)	13.8587(6)		13.8879(9)	
χ^2	1.63	1.55	1.59	

cubic crystal structure of MFO with the Fd-3m space group (PDF No. 04-013-6574). The obtained lattice parameters are presented in Table 1. Additionally, the average crystallite size calculated using the Debye-Scherrer equation was 36 nm.

After the synthesis of pure-phase BFO and MFO, nanocomposites of 50 % BFO and 50 % MFO were fabricated. The XRD patterns in Fig. 6(c) show that the nanocomposites retain the crystalline phase of the pristine components, as there are no new phases formed, and the major peaks of BFO and MFO are still observable without any peak shifting or phase transformation. The structural parameters of the rhombohedral BFO and cubic MFO crystals were well-preserved in the nanocomposites (Table 1), indicating that there had been no occurrence of structural changes during or after the fabrication. Since each component in the composite samples retained their own original crystal structures, the BFO-MFO composites could be considered to have been successfully fabricated.

3.3.2. Morphological properties

The TEM images of the BFO and MFO samples shown in Figs. 7(a-d) prove the formation of nanoparticles. Figure 7(a) confirms the polyshaped and agglomerated nanoparticles of BFO, which attributes are common in BFO samples fabricated by the sol-gel method [28, 34, 38]. The lattice spacing was calculated to be 2.743 Å (Fig. 7(b)), corresponding to the (110) plane of BFO. The particle size distribution, as seen in the inset of Fig. 7(b), showed that the particle size ranged from 25 to 150 nm with an average size of 93 nm.

The MFO appeared to be spherical and cubic in shape, as shown in Fig. 7(c). In the larger magnification of the TEM image (Fig. 7(d)), the MFO nanoparticles show distinct lattice fringes, confirming their high-crystalline nature. The calculated value of the d-spacing of one of the lattice fringes was about 1.627 Å, corresponding to the (511) plane. The particle size distribution was calculated to be 5 nm to 200 nm, and the average particle size was

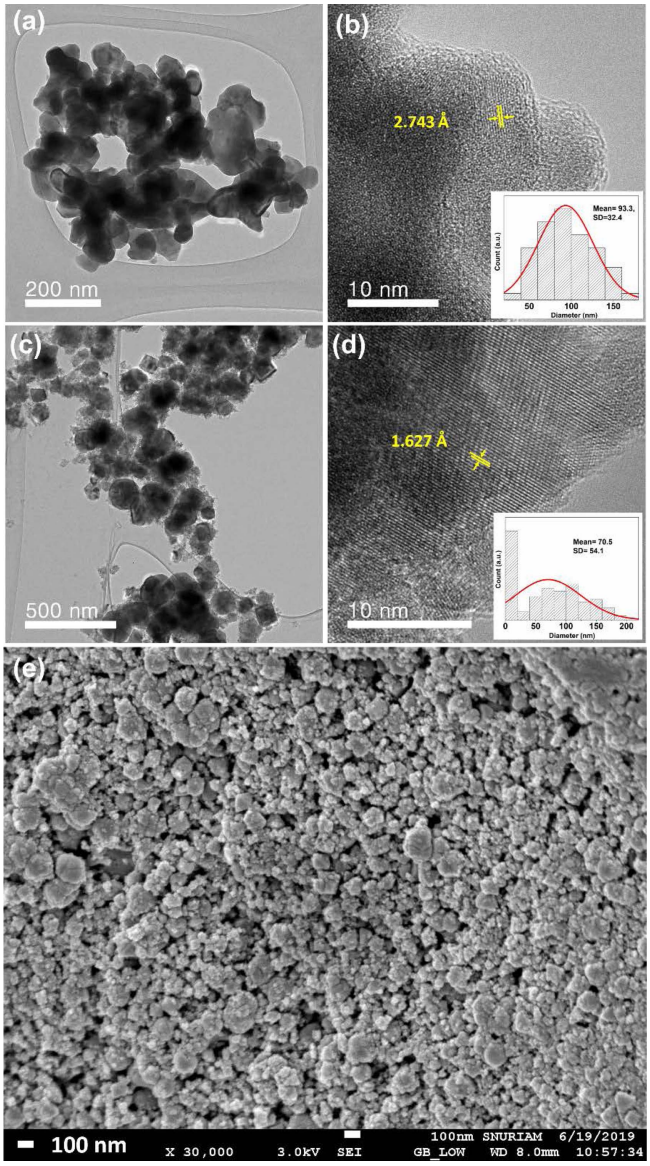

Fig. 7. (Color online) Bright-field TEM images of $BiFeO_3$ nanoparticles (a and b) and $MnFe_2O_4$ nanoparticles (c and d) with corresponding lattice images and particle size distributions, and SEM surface image of nanocomposites $MnFe_2O_4$-$BiFeO_3$ (e).

70.5 nm. Such a broad distribution of particle size is common for samples prepared by the co-precipitation method, because the nucleation and growth rates are not controlled during the synthesis.

The microstructure of the nanocomposite sintered in an N_2 atmosphere was characterized using secondary electron microscopy (SEM) imaging to obtain the surface image. Figure 7(e) shows that the composite was composed of nanoparticles of an approximate size of 100 nm. While pores could still be found, fewer and smaller pores were observed relative to the micro-size pores in an earlier report [21]. This could be achieved due to the use of nanoparticles as the precursor of the composite materials. Nanoparticles for composites possess more advantages due to their small size and large ratio of interface areas to volume, which reduce the inter-particle distance and increase the interfacial contacts between particles. A large interfacial area for each component nanoparticle is desired for magnetoelectric applications utilizing strain transfer from the ferroelectric to the ferromagnetic phase. Additionally, a dense and compact pellet was achieved at a lower sintering temperature (400 °C) compared with a previous report of the fabrication of a BFO and MFO nanocomposite that needed a very high sintering temperature up to 1000 °C [21].

3.3.3. Oxidation properties

The oxidation states of the pure phases of BFO and MFO and of the BFO-MFO composite were examined using XPS to confirm the phase purity and bonding characteristics of the samples. From the survey scan (Fig. 8(a)), the core-level peaks of Fe 2p, Mn 2p, and Bi 4f were fitted as shown in Figs. 8(b), (c) and (d), respectively. All of the binding energies of the observed peaks were adjusted with respect to the C 1s peak at 284 eV. In Fig. 8(b), the deconvolution of the Fe 2p peaks (magenta and blue lines) of the BFO sample shows the coexistence of Fe^{3+} and Fe^{2+}. Characteristic peaks for Fe^{3+} were found at 710.8 and 724 eV for the Fe $2p_{3/2}$ and Fe $2p_{1/2}$ peaks, respectively, and at around 718 and 733 eV for the satellite peaks. As for the presence of Fe^{2+}, characteristic peaks were observed at 709 and 722 eV for the Fe $2p_{3/2}$ and Fe $2p_{1/2}$ peaks, respectively. The presence of Fe^{2+} in the BFO system is common in sol-gel-derived BFO, due to the presence of oxygen defects [33, 34, 39]. On the other hand, the MFO sample showed no presence of Fe^{2+}, since only characteristic peaks of Fe^{3+} appeared. Additionally, the XPS spectra of the nanocomposite samples appeared to contain only the Fe^{3+}-characteristic peaks, even though the individual BFO sample showed some presence of Fe^{2+} peaks. This might have been caused by the major presence of Fe^{3+} instead of Fe^{2+} in the nano-

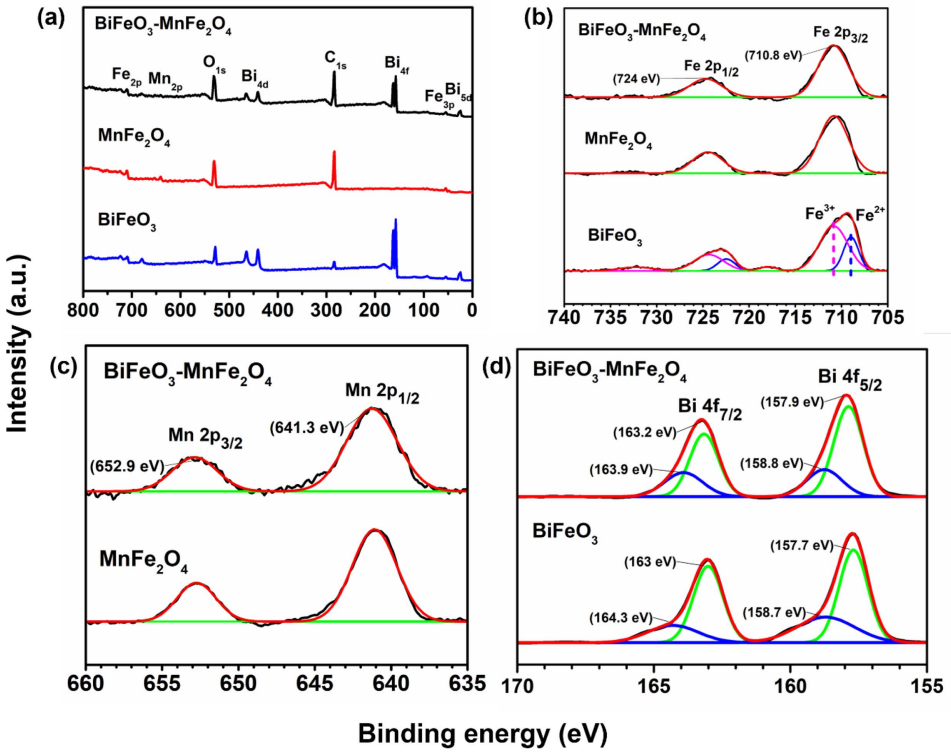

Fig. 8. (Color online) XPS spectra of $BiFeO_3$, $MnFe_2O_4$, and $BiFeO_3$-$MnFe_2O_4$ nanocomposites: (a) survey scan, (b) Fe 2p, (c) Mn 2p, and (d) Bi 4f peaks.

composites.

The XPS spectra of the MFO sample in Fig. 8(c) indicate the presence of the Mn^{2+} oxidation state. This could be determined from the characteristic peaks of Mn $2p_{3/2}$ at 641.3 eV, Mn $2p_{1/2}$ at 652.9 eV, and a particular satellite peak at 647 eV, which is not present in any of the other oxidation states of Mn. The XPS spectra of the nanocomposites revealed the same characteristic peaks as the MFO sample, which signified the existence of only Mn^{2+} in the nanocomposites.

Figure 8(d) shows the presence of Bi 4f doublet peaks in the BFO sample at 157.9 and 163.2 eV. Additionally, the spin-orbit splitting energy between the doublet peaks was calculated to 5.3 eV, which is very similar to the theoretical value of 5.31 eV [40]. This indicated the existence of Bi^{3+} in the system. Meanwhile, small subpeaks were observed in the BFO sample at around 163.9 and 158.8 eV, which may suggest the presence of Bi-O-Fe bonding at the octahedral site and/or the defect phase of Bi caused by oxygen vacancies [39, 41]. This result correlated with the Fe 2p XPS spectra, showing the presence of Fe^{2+} in the BFO caused by oxygen vacancies [31]. Additionally, the absence of peaks at 156 and 162 eV proved that there was no peak corresponding to Bi^0 [42]; hence, the Bi oxidation state in BFO was purely Bi^{3+}.

3.3.4. Magnetic Properties

The magnetic hysteresis (M-H) loops of the BFO, MFO and BFO-MFO nanocomposites are shown in Fig. 9. The hysteresis curve of pure BFO (black line) indicates a ferromagnetic and saturated feature, unlike bulk BFO with an unsaturated straight line, due to its antiferromagnetic properties [9]. The saturation magnetization (M_s) and coercivity (H_c) values of the pure BFO are 4.9 emu/g and 102.5 Oe, respectively, similar to the published results for the reported sol-gel synthesized BFO [27, 29]. Sol-gel synthesized BFO was found to have an increased M_s value due to the presence of oxygen vacancies and Fe^{2+} [6, 31, 43], iron oxide impurities [27] and internal stress [33, 44]. The enhancement of the saturation magnetization in our result was found to originate from the coexistence of Fe^{2+} and Fe^{3+}, which was discussed in the oxidation properties sub-section (3.3.3) above.

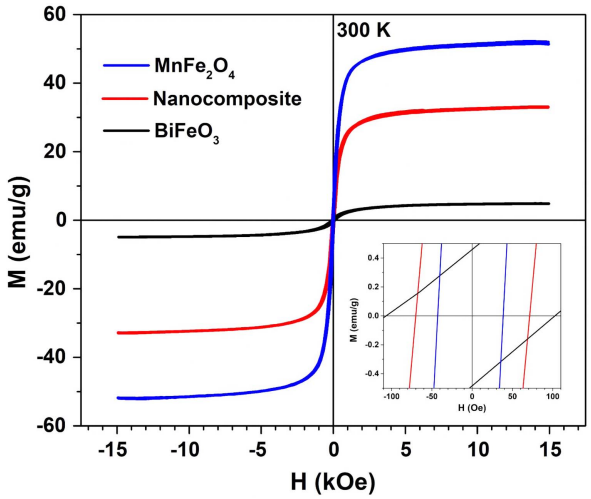

Fig. 9. (Color online) Magnetization hysteresis loops measured at 300 K. The inset shows the magnification of the hysteresis loops near coercivity values.

Figure 9's M-H loop of pure MFO nanoparticles (blue line) represents the M_s and H_c values of 52 emu/g and 38 Oe, respectively. Compared with other reports of similar synthesis methods [45, 46], our result showed a higher M_s value. In the inset in Fig. 9, it can be seen that the sample possessed a small coercivity, which is the typical characteristic of spinel ferrite materials. Smaller coercivity is a desirable ferromagnetic property for low-power-consumption magnetization switching [47].

The M-H loop of the BFO-MFO nanocomposites (red line) shows M_s and H_c values of 33 emu/g and 72 Oe, respectively. These results are similar to the M_s and H_c values approximated using Vegard's Law of approximation, 24.9 emu/g and 75 Oe, respectively. Compared with the bulk value of the M_s [21], our result showed an M_s enhancement.

4. Conclusion

The solvent condition and precursor amount in the sol-gel method were found to play a crucial role in the synthesis of pure single-phase $BiFeO_3$ nanoparticles. The saturation magnetization values of the $BiFeO_3$ nanoparticles were greatly enhanced due to the coexistence of Fe^{2+} and Fe^{3+} in the samples. Meanwhile, the preheating and aging steps were found to be prominent factors in the synthesis of pure-phase $MnFe_2O_4$ nanoparticles via the co-precipitation method. The synthesized pure-phase $BiFeO_3$ nanoparticles have a rhombohedral crystal structure of polyshape aspect, an average diameter of 93 nm, and a crystallite size of 31.9 nm. The cubic $MnFe_2O_4$ nanoparticles, on the other hand, are mostly nanospherical with an average size of 70.5 nm. The combination of these two materials was well fabricated as the Rietveld refinement results showed no changes in the crystal structures, thus proving a successful method for nanocomposite fabrication. The nanocomposites composed of 50 % $BiFeO_3$ and 50 % $MnFe_2O_4$ showed an enhanced saturation magnetization value (33 emu/g) compared to the pristine $BiFeO_3$ (4.9

emu/g), owing to the addition of magnetic $MnFe_2O_4$ nanoparticles. The value of 33 emu/g was significantly higher than the bulk values of BFO-MFO composite samples reported thus far. A comparatively low sintering temperature, 400 °C, which is desirable, also was achieved in this synthesis procedure.

Acknowledgments

This work was supported by the Basic Science Research Program through the National Research Foundation of Korea (NRF) funded by the Ministry of Science, ICT and Future Planning (Grant No. NRF-2018R1A2A1A05078913).

References

[1] T. Kimura, T. Goto, H. Shintani, K. Ishizaka, T. Arima, and Y. Tokura, Nature **426**, 55 (2003).
[2] S.-W. Cheong and M. Mostovoy, Nat. Mater. **6**, 13 (2007).
[3] J. F. Scott, J. Mater. Chem. **22**, 4567 (2012).
[4] M. Fiebig, T. Lottermoser, D. Meier, and M. Trassin, Nat. Rev. Mater. **1**, 16046 (2016).
[5] J. M. Moreau, C. Michel, R. Gerson, and W. J. James, J. Phys. Chem. Solids **32**, 1315 (1971).
[6] J. Wang, J. B. Neaton, H. Zheng, V. Nagarajan, S. B. Ogale, B. Liu, D. Viehland, V. Vaithyanathan, D. G. Schlom, U.V. Waghmare, N. A. Spaldin, K. M. Rabe, M. Wuttig, and R. Ramesh, Science **299**, 1719 (2003).
[7] I. Sosnowska, T. P. Neumaier, and E. Steichele, J. Phys. C **15**, 4835 (1982).
[8] D. Lebeugle, D. Colson, A. Forget, M. Viret, P. Bonville, J. F. Marucco, and S. Fusil, Phys. Rev. B **76**, 024116 (2007).
[9] T.-J. Park, G. C. Papaefthymiou, A. J. Viescas, A. R. Moodenbaugh, and S. S. Wong, Nano Lett. **7**, 766 (2007).
[10] S. K. Srivastav, N. S. Gajbhiye, and A. Banerjee, J. Appl. Phys. **113**, 203917 (2013).
[11] S. K. S. Patel, J.-H. Lee, M.-K. Kim, B. Bhoi, and S.-K. Kim, J. Mater. Chem. C **6**, 526 (2018).
[12] A. A. Belik, A. M. Abakumov, A. A. Tsirlin, J. Hadermann, J. Kim, G. Van Tendeloo, and E. Takayama-Muromachi, Chem. Mater. **23**, 4505 (2011).
[13] Q. Xu, H. Zai, D. Wu, T. Qiu, and M. X. Xu, Appl. Phys. Lett. **95**, 112510 (2009).
[14] K. G. Yang, Y. L. Zhang, S. H. Yang, and B. Wang, J. Appl. Phys. **107**, 124109 (2010).
[15] W. Mao, X. Wang, Y. Han, X. A. Li, Y. Li, Y. Wang, Y. Ma, X. Feng, T. Yang, J. Yang, and W. Huang, J. Alloys Compd. **584**, 520 (2014).
[16] G. S. Lotey and N. K. Verma, Journal of Materials Science: Materials in Electronics **24**, 3723 (2013).
[17] G. S. Lotey and N. K. Verma, Superlattices Microstruct. **60**, 60 (2013).
[18] J. S. Bangruwa, B. K. Vashisth, N. Singh, N. Singh, and V. Verma, J. Alloys Compd. **739**, 319 (2018).
[19] A. Das, S. De, S. Bandyopadhyay, S. Chatterjee, and D. Das, J. Alloys Compd. **697**, 353 (2017).
[20] H. Singh and K. L. Yadav, J. Alloys Compd. **585**, 805 (2014).
[21] A. Kumar and K. L. Yadav, Physica B **406**, 1763 (2011).
[22] G. Srinivasan, E. T. Rasmussen, J. Gallegos, R. Srinivasan, Y. I. Bokhan, and V. M. Laletin, Phys. Rev. B **64**, 214408 (2001).
[23] X. Qi, J. Dho, R. Tomov, M. G. Blamire, and J. L. MacManus-Driscoll, Appl. Phys. Lett. **86**, 062903 (2005).
[24] E. J. Holmyard, Text Book Inorganic Chemistry, Edward Arnold & Co., London, 1931.
[25] A. K. De, A Textbook of Inorganic Chemistry, 9 ed., New Age International Limited, New Delhi, 2003.
[26] P. Scherrer, Nachr. Ges. Wiss. Göttingen **26**, 98 (1918).
[27] S. Vijayanand, H. S. Potdar, and P. A. Joy, Appl. Phys. Lett. **94**, 182507 (2009).
[28] P. N. Francis, S. Dhanuskodi, M. S. Jayalakshmy, M. Muneeswaran, J. Philip, and N. V. Giridharan, Mater. Chem. Phys. **216**, 93 (2018).
[29] G. S. Lotey and N. K. Verma, J. Nanopart. Res. **14**, 742 (2012).
[30] F. Huang, Z. Wang, X. Lu, J. Zhang, K. Min, W. Lin, R. Ti, T. Xu, J. He, C. Yue, and J. Zhu, Sci. Rep. **3**, 2907 (2013).
[31] Y. Wang, Q.-h. Jiang, H.-c. He, and C.-W. Nan, Appl. Phys. Lett. **88**, 142503 (2006).
[32] R. Mazumder, P. S. Devi, D. Bhattacharya, P. Choudhury, A. Sen, and M. Raja, Appl. Phys. Lett. **91**, 062510 (2007).
[33] T. E. Quickel, L. T. Schelhas, R. A. Farrell, N. Petkov, V. H. Le, and S. H. Tolbert, Nat. Commun. **6**, 6562 (2015).
[34] S. K. S. Patel, J.-H. Lee, M.-K. Kim, and S.-K. Kim, J. Magnetics **24**, 371 (2019).
[35] B. Jeyadevan, C. N. Chinnasamy, K. Shinoda, K. Tohji, and H. Oka, J. Appl. Phys. **93**, 8450 (2003).
[36] N. A. Frey, S. Peng, K. Cheng, and S. Sun, Chem. Soc. Rev. **38**, 2532 (2009).
[37] C. N. Chinnasamy, B. Jeyadevan, O. Perales-Perez, K. Shinoda, K. Tohji, and A. Kasuya, IEEE Trans. Magn. **38**, 2640 (2002).
[38] T. Gao, Z. Chen, Y. Zhu, F. Niu, Q. Huang, L. Qin, X. Sun, and Y. Huang, Mater. Res. Bull. **59**, 6 (2014).
[39] S. Bharathkumar, M. Sakar, and S. Balakumar, J. Phys. Chem. C **120**, 18811 (2016).
[40] R. Nyholm, A. Berndtsson, and N. Martensson, J. Phys. C **13**, L1091 (1980).
[41] Z. Quan, H. Hu, S. Xu, W. Liu, G. Fang, M. Li, and X. Zhao, J. Sol-Gel Sci. Technol. **48**, 261 (2008).
[42] S. Chaturvedi, I. Sarkar, M. M. Shirolkar, U.-S. Jeng, Y.-Q. Yeh, R. Rajendra, N. Ballav, and S. Kulkarni, Appl. Phys. Lett. **105**, 102910 (2014).
[43] W. Eerenstein, F. D. Morrison, J. Dho, M. G. Blamire, J. F. Scott, and N. D. Mathur, Science **307**, 1203 (2005).

[44] Y. Wu, J.-g. Wan, C. Huang, Y. Weng, S. Zhao, J.-m. Liu, and G. Wang, Appl. Phys. Lett. **93**, 192915 (2008).
[45] U. Lamdab, K. Wetchakun, W. Kangwansupamonkon, and N. Wetchakun, RSC Adv. **8**, 6709 (2018).
[46] P. Iranmanesh, S. Saeednia, M. Mehran, and S. R. Dafeh, J. Magn. Magn. Mater. **425**, 31 (2017).
[47] X.-M. Liu, S.-Y. Fu, and C.-J. Huang, Mat. Sci. Eng. B **121**, 255 (2005).